



HAL
open science

Membrane behavior of uni- and bidirectional non-crimp fabrics in off-axis-tension tests

Bastian Schäfer, Ruochen Zheng, N Naouar, Luise Kärger

► **To cite this version:**

Bastian Schäfer, Ruochen Zheng, N Naouar, Luise Kärger. Membrane behavior of uni- and bidirectional non-crimp fabrics in off-axis-tension tests. *International Journal of Material Forming*, 2023, 16 (6), pp.68. 10.1007/s12289-023-01792-x . hal-04258307

HAL Id: hal-04258307

<https://hal.science/hal-04258307v1>

Submitted on 25 Oct 2023

HAL is a multi-disciplinary open access archive for the deposit and dissemination of scientific research documents, whether they are published or not. The documents may come from teaching and research institutions in France or abroad, or from public or private research centers.

L'archive ouverte pluridisciplinaire **HAL**, est destinée au dépôt et à la diffusion de documents scientifiques de niveau recherche, publiés ou non, émanant des établissements d'enseignement et de recherche français ou étrangers, des laboratoires publics ou privés.



Membrane behavior of uni- and bidirectional non-crimp fabrics in off-axis-tension tests

Bastian Schäfer¹ · Ruochen Zheng² · Naim Naouar² · Luise Kärger¹

Received: 15 August 2023 / Accepted: 2 October 2023
© The Author(s) 2023

Abstract

The production of high-performance composite parts with non-crimp fabrics (NCFs) requires a profound understanding of the material's behavior during draping to prevent forming defects such as wrinkling and gapping. Simulation methods can be used to model the complex material behavior of NCFs and predict their deformation during the draping process. However, NCFs do not intrinsically deform under pure shear like most woven fabrics, but often under superimposed shear, transverse tension and in-plane roving compaction. Therefore, non-standard characterization methods have to be applied besides typical picture frame tests or bias-extension tests. Off-axis-tension tests (OATs) utilize a simple setup to characterize a fabric's membrane behavior under different ratios of superimposed shear, transverse tension and in-plane compaction. OATs at three different bias angles (30°, 45° and 60°) are conducted to investigate a unidirectional and a bidirectional NCF. A method is presented to measure the fiber curvatures in addition to the occurring strains. The investigations reveal a relatively symmetrical, shear-dominated behavior with limited roving slippage for the Biax-NCF. The behavior of the UD-NCF strongly depends on the stitching load during tests and is characterized by an asymmetric shear behavior as well as significant roving slippage. The off-axis-tension test results can be used as the basis for the development and validation of new simulation methods to model the complex membrane behavior of NCFs.

Keywords Fabrics/textiles · UD- and Biax-NCF · Mechanical properties · Forming

Introduction

Non-crimp fabrics (NCFs) can be used in liquid composite molding processes to manufacture high-performance components utilized in the automotive or aerospace sectors. Their straight fibers provide a higher lightweight potential compared to woven fabrics with undulated fibers. They are made

of one (UD-NCF), two (Biax-NCF) or more directions of fibers linked together with a polymer stitching. The deformation behavior of NCFs is challenging and they are more susceptible to effects like gapping, rovings sliding and fiber waviness compared to woven fabrics [1–5]. Therefore, a comprehensive characterization of their deformation behavior is essential to model their forming behavior in draping simulations [6–8].

The membrane behavior of fabrics has mainly been characterized with the picture frame (PFT) or bias-extension test (BET) [3, 9–15]. The PFT induces a pure shear by deforming the fabric in a square-hinged frame to a rhomboid. The BET is a tensile test on a rectangular specimen with the fibers oriented at an offset angle of 45°. This results in three distinct deformation zones with a shear-dominated main deformation zone (MDZ) in the specimen's center. For woven fabrics, both setups were extensively studied and theoretical descriptions of their shear deformation were developed together with normalization methods to compare them under the assumptions of inextensible fibers, no slippage and pure shear [9, 13, 16–20]. Under proper initial placements of the specimens

✉ Bastian Schäfer
bastian.schaefer@kit.edu

✉ Luise Kärger
luise.kaerger@kit.edu
Ruochen Zheng
ruochen.zheng@insa-lyon.fr
Naim Naouar
naim.naouar@insa-lyon.fr

¹ Lightweight Engineering, Institute of Vehicle System Technology (FAST), Karlsruhe Institute of Technology (KIT), Karlsruhe 76131, Germany

² LaMCoS, CNRS, Université de Lyon (INSA Lyon), Lyon F-69621, France

and prevention of fiber tension during the PFT, comparable results for both tests were achieved even for different specimen sizes [9]. The normalized results of both tests can be directly incorporated into forming simulations based on a pure shear assumption [11, 21–23].

However, NCFs do not intrinsically deform under pure shear, which leads to significant differences in the results of BETs and PFTs in the case of Biax-NCF [12, 24, 25] as well as UD-NCF [15, 26]. This is most notable in a comparison of the theoretical and measured shear angle [24, 27]. NCFs deform under a combination of relative fiber rotation (pure shear) and slippage between fiber rovings (simple shear) as well as the different fiber layers [28–30]. This specific deformation behavior together with an easier setup made the BET more commonly used for Biax- [24, 25, 27, 31–35] and UD-NCF [15, 26, 27, 36–40] compared to the PFT [24, 25, 41–43].

Pourtier et al. [34, 44] proposed an alternative method to investigate the deformation of NCFs in the BET under the assumption of simple shear, which is a macroscopic description of slippage for UD materials. For the investigated Biax-NCF the main deformation mode was slippage (simple shear) during the test's beginning and changed to rotation of the fibers (pure shear). Krogh et al. [45] combined the pure and simple shear theories with the observations of Harrison et al. [18] that the relative slip can be estimated by the specimen width at half height. For the investigated quasi-UD-NCF, a transition from pure to simple shear was observed and the shear angle could be predicted based on the width. The deformation behavior of NCF strongly depends on the material architecture, fiber and stitching type [46, 47]. Therefore, there is currently no universal method for the characterization of the membrane behavior of NCFs available.

Schirmaier et al. [36] and later Ghazimoradi et al. [39] conducted so-called off-axis-tension tests (OATs) with fiber angles of 30° and 60° in addition to BETs to characterize different ratios of superimposed transverse tensile and shear deformation of a UD-NCF. Macroscopic forming simulation models parametrized based on those OATs showed better agreement with component forming tests, compared to a parameterization based on PFT for pure shear deformation and uniaxial tensile tests perpendicular to the fiber rovings for transverse tensile deformation [36, 40]. This highlights the complex deformation behavior under different multi-axial strain conditions, where an exclusive consideration of the shear behavior is not sufficient during characterization [26, 39, 40]. Additionally, the test setup for OATs is relatively simple and widely available compared to, for example, multi-axial testing machines otherwise necessary to study different ratios of superimposed strains [48].

In addition, existing theoretical investigations concerning the deformation during BETs neglect mesoscopic effects like the in-plane fiber bending. These manifest in the form of transitioning zones between different shear zones instead of sharp changes assumed in kinematic models or theories based on classical continuum theories [6, 32, 49]. In order to model this effect, generalized continuum approaches are necessary [12]. Ferretti et al. [49] and Steer et al. [50] used a second-order gradient theory to model the influence of the fiber bending stiffness on the size of the transitioning zones and magnitude of the resulting fiber curvature. However, the results were not quantitatively validated since no method for the experimental measurement of in-plane bending is reported in the literature.

Since NCFs do not adhere to theoretical kinematic models, Boisse et al. [12] recommended in their review paper to measure the deformation independent of the machine displacement. Commonly the shear strain has been measured during the BET via DIC [14, 32, 37, 45, 51] or other discrete methods based on individual measurement points [52] or lines [13, 17, 20, 34, 53]. Thereby, the influence of the measuring system is often neglected in literature but can have a significant influence on the deformation as demonstrated by Trejo et al. for UD-NCF [37].

In this study, the membrane behavior of a UD- and Biax-NCF is investigated in off-axis tension tests (OATs) of three different bias angles (i.e. 30°, 45° and 60°). A dot pattern aligned with the rovings is applied to the specimens, enabling a macroscopic strain measurement using DIC. Furthermore, a method is presented to measure in-plane roving bending based on the curvature in fiber direction. The influence of the measuring method is evaluated based on the impact on the resulting process forces and discrete measurements of the fiber orientation and deformed sample width. Finally, implications regarding the relevance of the individual experiments for a comprehensive characterization of the membrane behavior for forming simulations are discussed.

Material

In this study, a unidirectional (UD300) and a bidirectional (MD600) non-crimp fabric (NCF) both without binder are used, cf. Fig. 1. The fabrics are manufactured by Zoltek™ and produced from their PX35-50K continuous carbon (CF) fiber heavy tows. Both fabrics are stitched together with a 76 dtex PES yarn in a Tricot pattern. The UD300 consists of a single layer of aligned CF rovings with thin glass fibers (GF) on the back for improved handleability. The MD600 consists of two layers in a 0°/90° orientation. Both fabrics

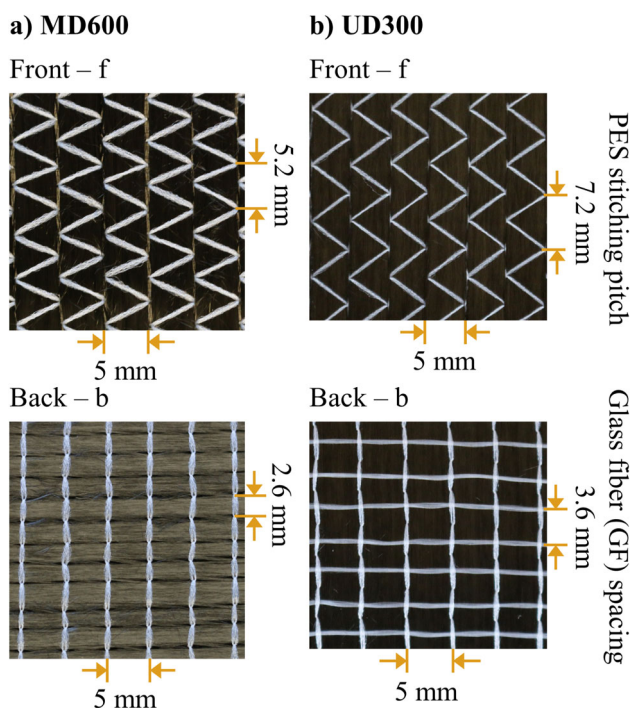


Fig. 1 (a) Bidirectional ($0^\circ/90^\circ$) NCF MD600 and (b) unidirectional NCF UD300 and

have a similar number of CFs in each layer with about 300 gm^{-2} in their respective main reinforcing directions.

Experimental test setup and procedure

Experimental setup

A Zwick-Roell Z2.5 universal testing machine with a 500 N load cell is used to conduct all tests at room temperature. All specimens were prepared from the same roll of UD- and Biax-material on an automated cutting table by Zünd Systemtechnik AG, Altstätten, Switzerland. Only samples that did not have damaged stitching or frayed fibers at the edges after cutting were selected. The OATs were performed on the UD-NCF for three different bias angles (i.e. 30° , 45° and 60°) and on the Biax-NCF for 30° as well as 45° . These bias angles were selected to impose different ratios of in-plane shear and tensile strains based on the results of the study by Schirmaier et al. [36]. An aspect ratio $a = l_0/w_0 = 2$ with an initial specimen length l_0 of 320 mm and width w_0 of 160 mm was used with a velocity of $v = 60 \text{ mm/min}$, cf. Fig. 2. Each test was repeated five times for each configuration with and without a dot pattern.

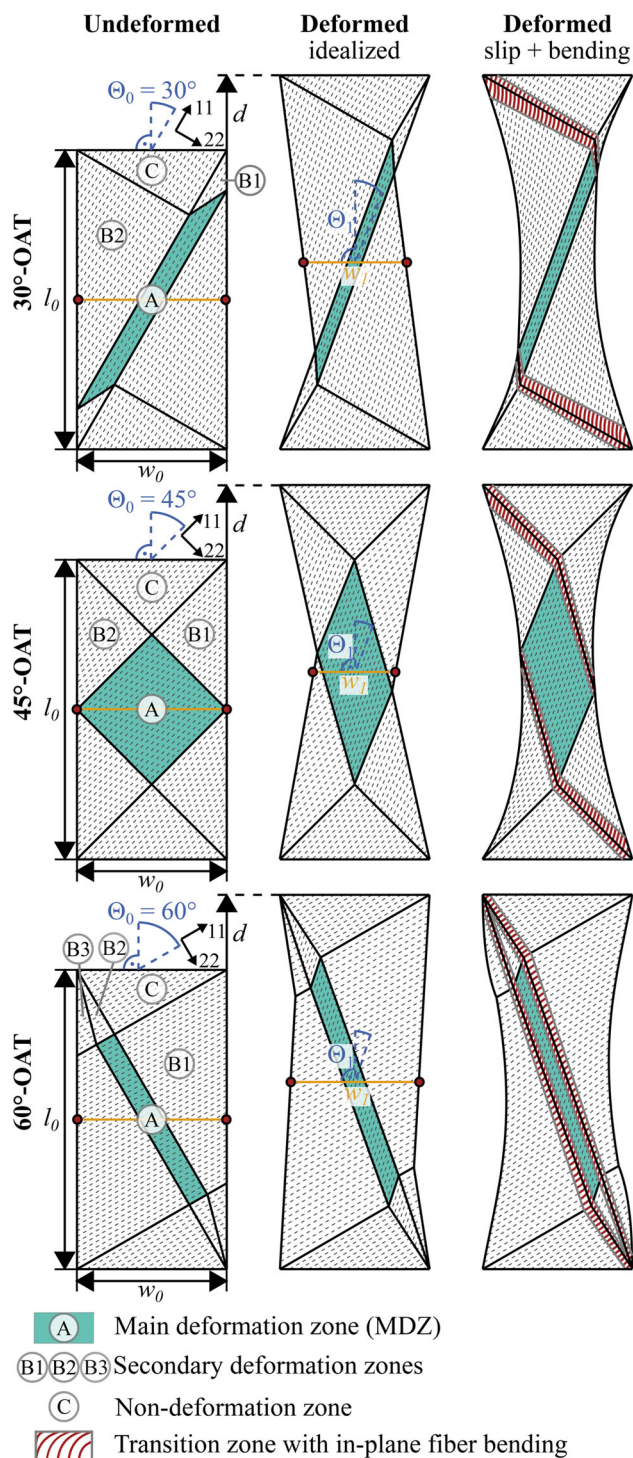


Fig. 2 30° , 45° and 60° -Off-Axis-Tensions tests (OATs) - Undeformed geometries, idealized deformed specimens and deformed specimens taking into account fiber slip and bending deformation in the transition zones

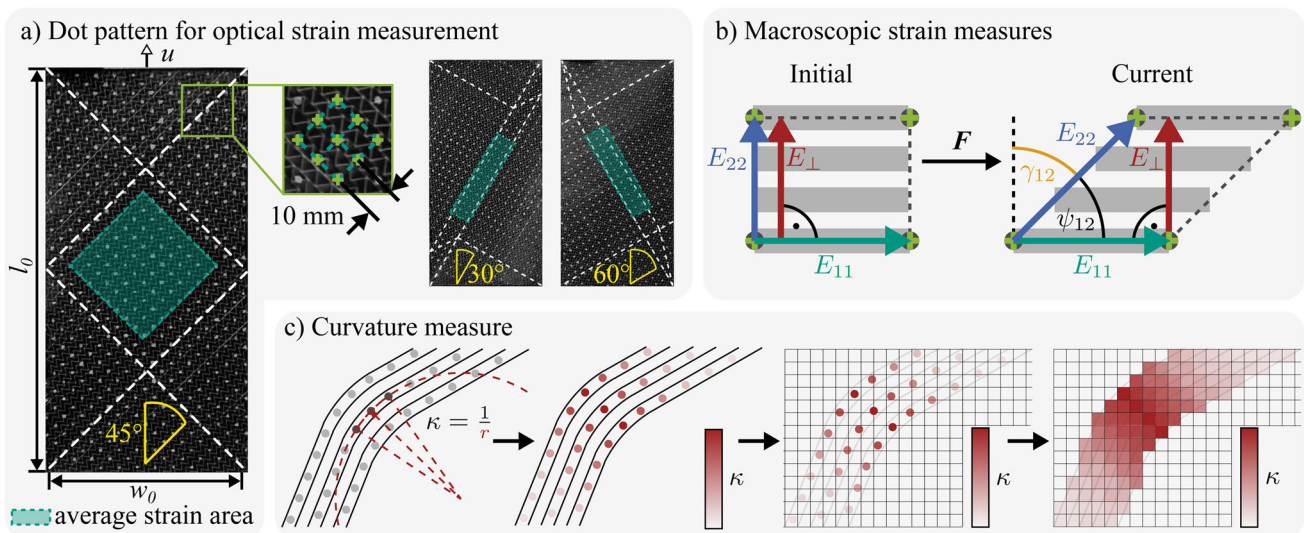


Fig. 3 (a) Dot pattern utilized during 2D-DIC to measure (b) macroscopic strains as well as (c) resulting curvature in fiber direction

Macroscopic strain and curvature measurement method

The macroscopic deformation is measured via Digital Image Correlation (DIC). A regular grid of white dots of acrylic paint with an approximate diameter of 2 mm is applied to the specimens using a stencil with a distance of $l_e = 10, mm$, c.f. Fig. 3a. Acrylic paint was used because other white markers, paint colors, or spray paints either soaked strongly into the fabric or had too little contrast on the rovings compared to the seams. The grid is aligned with the principle fiber direction during the test and each dot is manually positioned as centered as possible on the rovings. The deformation is recorded with a Canon EOS 70 D DSLR camera at 30 frames per second. The displacement of each dot was tracked with an open-source MathWorks Matlab DIC tool [54], which was enhanced to account for the regular grid [15, 36]. Subsequently, four dots are combined into a 2D quadrilateral element and the deformation gradient F rotated in the initial

fiber direction is calculated based on linear shape functions [55].

During the tests, especially for UD-NCF, large shear strains superimposed with transverse tensile deformation in the stitching direction and compression perpendicular to the carbon fiber rovings are expected on a macroscopic level [36, 40]. Therefore, in addition to the the Green-Lagrange strains E , the shear angle γ_{12} is calculated according to

$$\gamma_{12} = \frac{\pi}{2} - \psi_{12} = \frac{\pi}{2} - \arccos\left(\frac{C_{12}}{\sqrt{C_{11}}\sqrt{C_{22}}}\right), \quad (1)$$

and a strain perpendicular to the carbon fibers E_{\perp}

$$E_{\perp} = \sqrt{2 E_{22} + 1} \sin(\psi_{12}) - 1, \quad (2)$$

where C is the right Cauchy-Green tensor and ψ_{12} is the current angle between the principle directions, cf. Fig. 3b. The non-orthogonal orientation of the principale directions under large deformations (material frame) is intrinsically

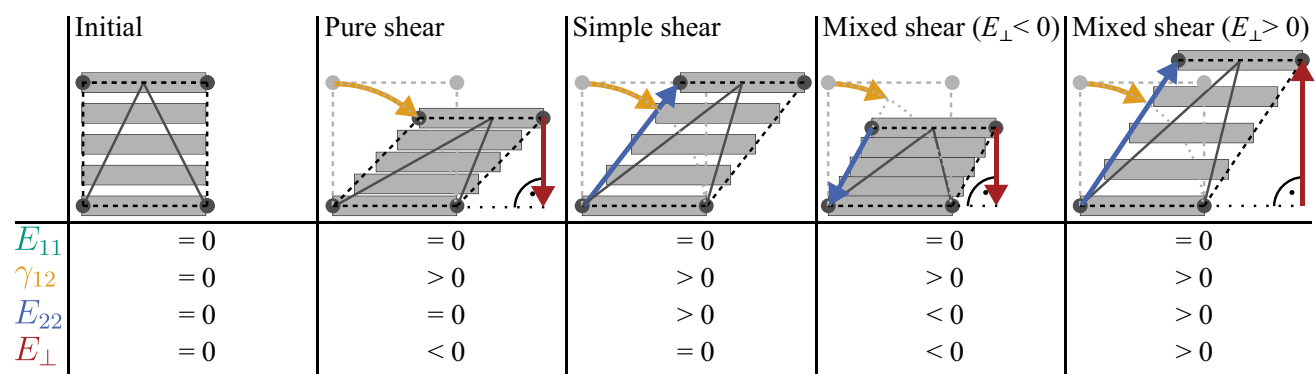


Fig. 4 Schematical representation of different deformation modes and the corresponding resulting strains

considered by the Green-Lagrange strains, since the coordinate system is initially aligned with the fiber direction, cf. Fig. 2.

These strain measurements, combined with the regular grid pattern of dots aligned with the rovings, allow distinction between different deformation modes, cf. Fig. 4. In the case of pure shear, E_{22} is zero and thus E_{\perp} is directly coupled to γ_{12} , cf. Eq. 2, while both strains are independent of each other for mixed shear. The perpendicular strain measures the distance between rovings and thus allows identifying gapping ($E_{\perp} > 0$) as well as compression of rovings ($E_{\perp} < 0$). Positive transverse tensile strains $E_{22} > 0$ indicate slippage parallel to the rovings but not necessarily gapping as is evident, for example, for simple shear. For a quantitative evaluation of the strain development during the tests, the strains in the main deformation zone (MDZ) are averaged over the areas highlighted in Fig. 3a.

To investigate fiber bending, a method to measure the curvature κ_{11} in fiber direction on a macroscopic scale is proposed, cf. Fig. 3 c. All dots along an individual fiber

roving are interpolated as a smoothed spline using Matlab's "Curve Fitting Toolbox™". For each roving 100 uniformly distributed points are derived to increase the resolution and compensate for placement inaccuracies of dots deviating from the roving's center. The curvature at each point is calculated based on the inverse radius of a circle placed through the point and both neighbors. Finally, the curvatures are linearly interpolated onto an evenly distributed 100x100 grid.

Results and discussion

Kinematic analysis of OATs

Figure 2 presents schematic illustrations of undeformed and deformed specimens of unbalanced fabrics during OATs. Three distinct types of zones are identifiable independent of the bias angle. In zone "C" the fibers are clamped along one edge and barely deform during the test. Zone "A" does not share a boundary with "C" and fibers passing through it are free on both edges. Therefore, the largest deformations in the form of fiber slippage (simple shear) and rotation (pure shear) occur in this main deformation zone (MDZ). Depending on the initial orientation, fibers in zones "B" pass through either "A" or "C", thus these areas must be distinguished more precisely [34]. The fibers in zones "B2" are subjected to a force perpendicular to their orientation due to the deformation in "A". This causes them to rotate and remain relatively parallel to the fibers in "A". The fibers in zone "B1" are strained along their orientation which causes them to slide relative to each other and remain similarly oriented to the fibers in zone C. In fibers in zone "B3" during the 60°-OAT behave similarly to those in "B1". Zones "B1" and "B2" are more distinct from each other for highly unbalanced textiles such as UD-NCF than for Biax-NCF.

In idealized models based on classical continuum mechanics, all zones are sharply defined without transition zones and the relative fiber slip is limited resulting in straight outer contours, cf. Fig. 2 [13, 53]. However, general slippage between the fibers and stitching as well as highly localized slippage at the boundaries from zones "A" to "B", results in a curved outer contour. Additionally, transition zones with high in-plane fiber curvatures form between the zones "C" to "B2" as well as "B1" to "A". The size of the transition zones depends on the in-plane bending stiffness of the fibers [49].

Machine forces

To investigate the influence of the dot pattern on the deformation behavior, the tests were performed both with and without dots on the front (f) side of all specimens. Additionally, the

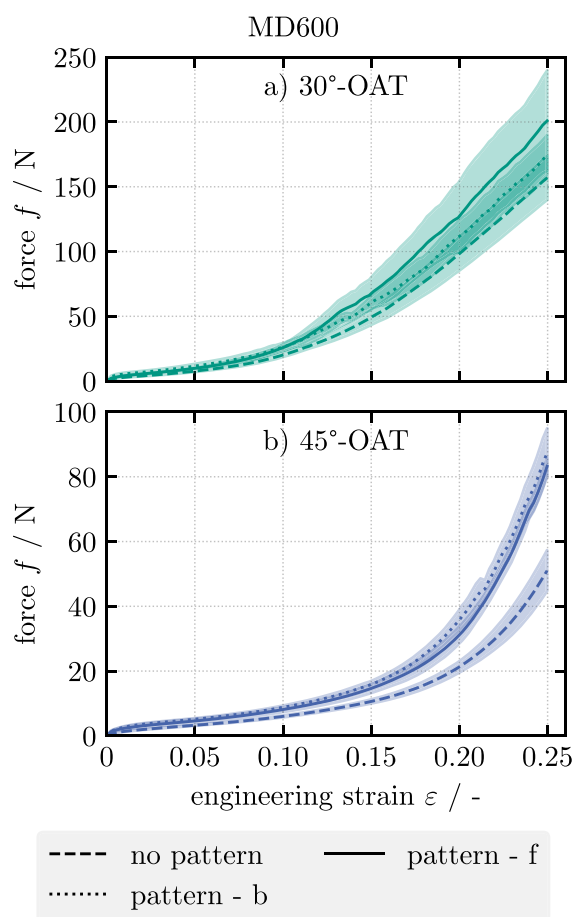


Fig. 5 Forces in the (a) 30°- and (b) 45°-OATs for medium-sized specimens (320 x 160 mm) of the Biax-NCF (MD600) with and without a dot pattern on the front (f) or the back (b)

tests were performed with dot patterns on the back (b) side for the Biax-NCF and the 45°-OAT for the UD-NCF.

The resulting machine forces for the Biax-NCF are shown in Fig. 5 and for the UD-NCF in Fig. 6. Normalization of the results was deliberately omitted in this section since the common assumption of a symmetrical deformation in the 45°-OAT is not fulfilled for unbalanced fabrics and the methods are not directly transferable for the 30°- and 60°-OAT [53].

The Biax-NCF curves can be divided into two sections, a relatively linear increase at the beginning and a stronger force increase (locking) for larger strains, cf. Fig. 5. The onset of locking is significantly earlier at $\varepsilon \approx 0.1$ for the 30°-OAT compared to $\varepsilon \approx 0.16$ for the 45°-OAT. This results from a higher localization of strain in a smaller MDZ and, together with the stronger orientation in load direction, leads to significantly higher forces in the 30°-OAT.

The application of a dot pattern on the front or back of the specimen increases the measured forces for the Biax-NCF, cf. Fig. 5. The acrylic paint mechanically reinforces the fabric and introduces additional adhesion between the fibers and stitching. This effect is more pronounced with a higher variation for a pattern on the front of the fabric in the 30°-OAT, since the zigzag pattern of the tricot stitch is covered more often by the dots compared to the straight stitch constellation on the backside, cf. Fig. 1a. Besides the increased forces, the general progressions of the curves with and without patterns are similar to each other with similar transition points between the different curve regions.

In the 45°-OAT for the UD-NCF, the dot pattern was applied either on the front or back. However, this caused the glass fibers and rovings to stick together at the dots on the back, resulting in significantly higher forces, cf. Fig. 6b. Furthermore, the distinction between the white dots and glass fibers was problematic for the DIC algorithm resulting in a worse correlation for high deformations. Therefore, the dot patterns were only applied on the front side of the UD-NCF for the other bias angles.

The UD-NCF curves can be divided into three sections, a relatively linear increase at the beginning, followed by a region with a decreased slope and locking for larger strains, cf. Fig. 6. Similar to the Biax-NCF, these sections are small in the 30°-OAT due to the localized deformation in a small MDZ. However, the dot pattern results in an earlier onset of locking and a slight drop in the forces with high variation for $\varepsilon \approx 0.2$ as the bond between the paint, stitching, and rovings tears loose. The forces during the 45°- and 60°-OAT are in the same order of magnitude despite the different bias angles. However, the stitching in the early phase of the 60°-OAT is under higher tension compared to more roving rotation and sliding in the 45°-OAT, resulting in a higher initial linear slope. The transition to the second, shear-dominated, phase with a distinctively shaped MDZ occurs at a similar engineer-

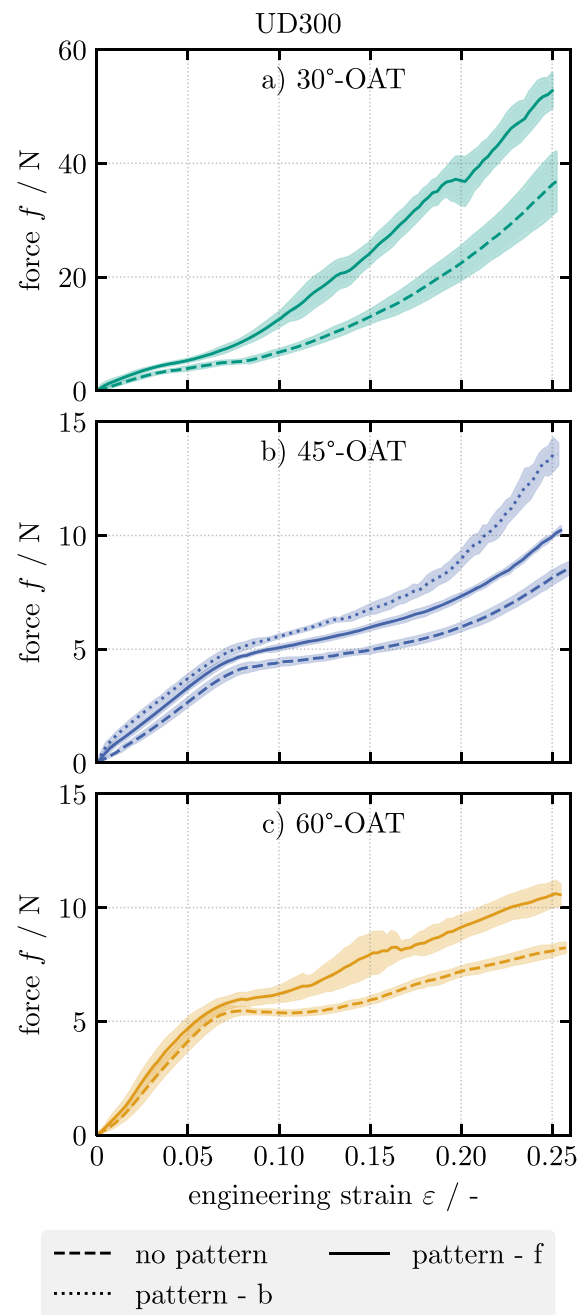


Fig. 6 Forces in the (a) 30°, (b) 45°- and (c) 60°-OATs for medium-sized specimens (320 x 160 mm) of the UD-NCF (UD300) with and without a dot pattern on the front (f) or the back (b)

ing strain of $\varepsilon \approx 0.075$ for both tests. The secondary slope in the 60°-OAT without a dot pattern is slightly negative before an early onset of locking after $\varepsilon \approx 0.12$. This transition is barely noticeable for the dot pattern applied on the front. The acrylic paint leads to a stronger adhesion between the rovings and stitching, making it more resistant to mutual slippage. This also results in a higher variation, as the stitching tears loose for higher forces.

Observed deformation and impact of the DIC

Due to the observed increase in the measured machine force, cf. Section 4.2, the influence of the dot pattern required for DIC during the OATs on the deformation behavior must be estimated. A qualitative comparison of the video recordings of tests with and without the dot pattern did not show any noticeable differences and a similar deformation was observed, as exemplarily shown by the images at a displacement of 80 mm in Fig. 8. To quantitatively confirm this observation, for three tests of each configuration with and without a dot pattern, image analysis was used at a displacement of 20, 40, 60 and 160 mm to measure the roving orientation Θ_n relative to the vertical axe at three positions in the MDZ and the relative necking Δw_n , cf. Fig. 7.

The fiber orientation was chosen because only one layer of rovings is visible on each side and significant slippage between the rovings and stitching is observed, making a direct estimation of the shear angle or other strains impossible from individual images. The relative necking is calculated from the initial w_0 and current w_1 width at half specimen height according to

$$\Delta w_n = \frac{w_0 - w_1}{w_0}. \quad (3)$$

Krogh et al. [38] have shown for a quasi UD-NCF that the necking in the 45°-OAT directly correlates with the shear strain development and can even be used for its estimation based on a scaled combination of pure and simple shear theory. The results for the Biax-NCF and UD-NCF are shown in

Fig. 7, together with the theoretical values according to pure shear and simple shear theory as derived by Krogh et al. [38] for the 45°-OAT.

The relative necking Δw_n of the Biax-NCF is similar in the 30°- and 45°-OATs, cf. Fig. 7a. In the 30°-OAT the application of the dot pattern on the front or back of the fabric has no significant influence on Δw_n . In the 45°-OAT about ~ 4 % more necking is measured with a dot pattern on either side. These observations are also reflected in the roving orientation. Similar to Krogh et al. [38], the development of the relative necking in the 45°-OAT strongly correlates with the resulting roving orientation and remains between the theoretical results for pure and simple shear. Overall, the application of the dot pattern has very little effect on the deformation behavior of the Biax-NCF and only slightly increases shear due to fiber rotation in the 45°-OAT.

In the case of the UD-NCF, the relative necking and roving orientation are only minimally affected by applying the dot pattern on the front during the 30°- and 45°-OATs, cf. Fig. 7b. Applying the dot pattern on the back increases the relative necking noticeably, similar to the impact on the required machine force, cf. Section 4.2. However, the roving orientation in the MDZ decreases only slightly, indicating that the deformation in this area remains similar. Taking a closer look at the images of the specimens in Fig. 2, gaps between the rovings in the edge areas of zones "B1" and "B2" can be identified in tests without a dot pattern or with a pattern on the front. At the dots on the back, the glass fibers and the rovings stick together, which prevents the glass fibers from slipping and inhibits the formation of gaps in the edge areas. In the 60°-OAT, the application of the pattern on the front

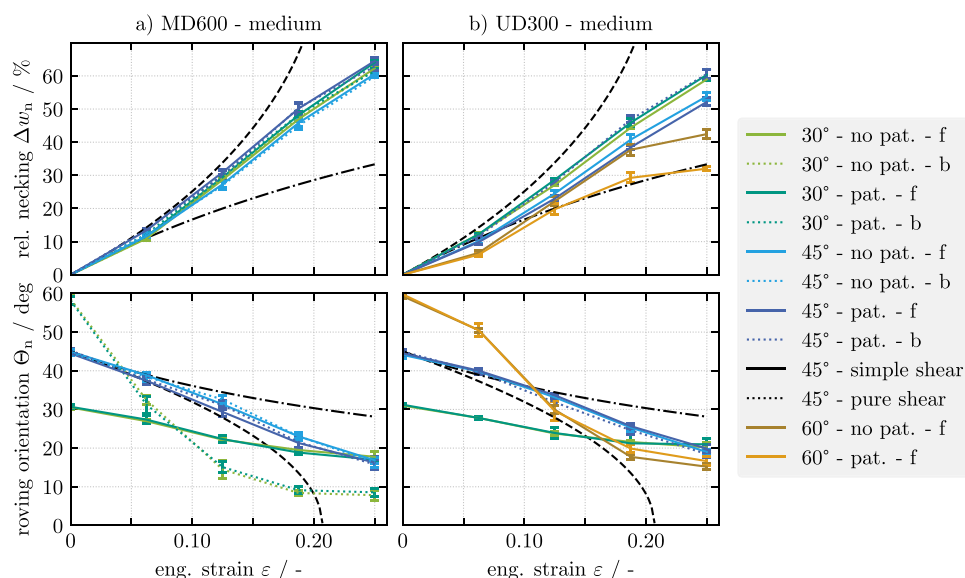


Fig. 7 Relative necking Δw_n and roving orientation Θ_n in the MDZ of the OATs for the (a) Biax-NCF and (b) UD-NCF for all tests with and without a dot pattern (pat.) on the front (f) or back (b) of the medium-sized specimens (320 x 160 mm)

significantly reduces Δw_n , compared to only slightly higher Θ_n in the MDZ for larger engineering strains. Analyzing the images of the 60°-OAT, the rovings in the zone "B1" of tests without a dot pattern, especially around half height of the specimen, are less rotated towards the load direction (larger Θ_n), indicating less shear deformation in these areas. This shear deformation is increased in tests with a dot pattern, since the additional adhesion between the rovings and stitching probably prevents relative slippage between them, resulting in more fiber rotation (pure shear).

In conclusion, the dot pattern required for DIC has little influence on the deformation of the Biax-NCF in general and should be applied to the front of the UD-NCF to reduce its impact. However, the effect on the deformation in the MDZ appears to be minimal for all tests, as indicated by the similar roving orientations with often overlapping scatter. Comparing the utilized point-based method, with the methods investigated by Trejo et al. [37], it is evident how small the influence is due to the minimal surface area of the fabric that is covered by paint. Trejo et al. compared three traditional areal speckle patterns from different paint types for DIC on a very similar UD-NCF in the 45°-OAT. Although their method achieved a higher resolution, the measured force already increased by $\sim 50\%$ and the estimated shear strain

in the MDZ decreased by $\sim 25\%$ even for the best of the investigated patterns at $\varepsilon \approx 0.14$.

Macroscopic strains measured with DIC

The resulting strains and roving curvature measured by DIC as described in Section 3.2 are shown in Fig. 8. The measured strains in the visible fiber direction E_{11} were negligible due to the high fiber stiffness and therefore not discussed in the following. For all tests, the different zones shown in Fig. 2 and described in Section 4.1 are distinguishable. The highest shear angles γ_{12} occur in the MDZ for all bias angles together with significant perpendicular compressive strains E_{\perp} .

The Biax-NCF has a relatively symmetric shear behavior in the 45°-OAT, compared to the UD-NCF with a smaller shear angle in zone "B2" than "B1". In the 30°-OAT, large transverse tensile strains E_{22} occur in the MDZ on the front for both materials. In conjunction with large positive γ_{12} , E_{\perp} and negative E_{22} strains in the adjacent zones "B2", these indicate significant relative roving slippage. Similar, but less pronounced, behavior is observable in the transition zones between "A" and "B2" of the 45°-OATs. In contrast, large transverse tensile strains E_{22} along with positive perpendicular strains E_{\perp} occur in the edge regions of zones "B2" in

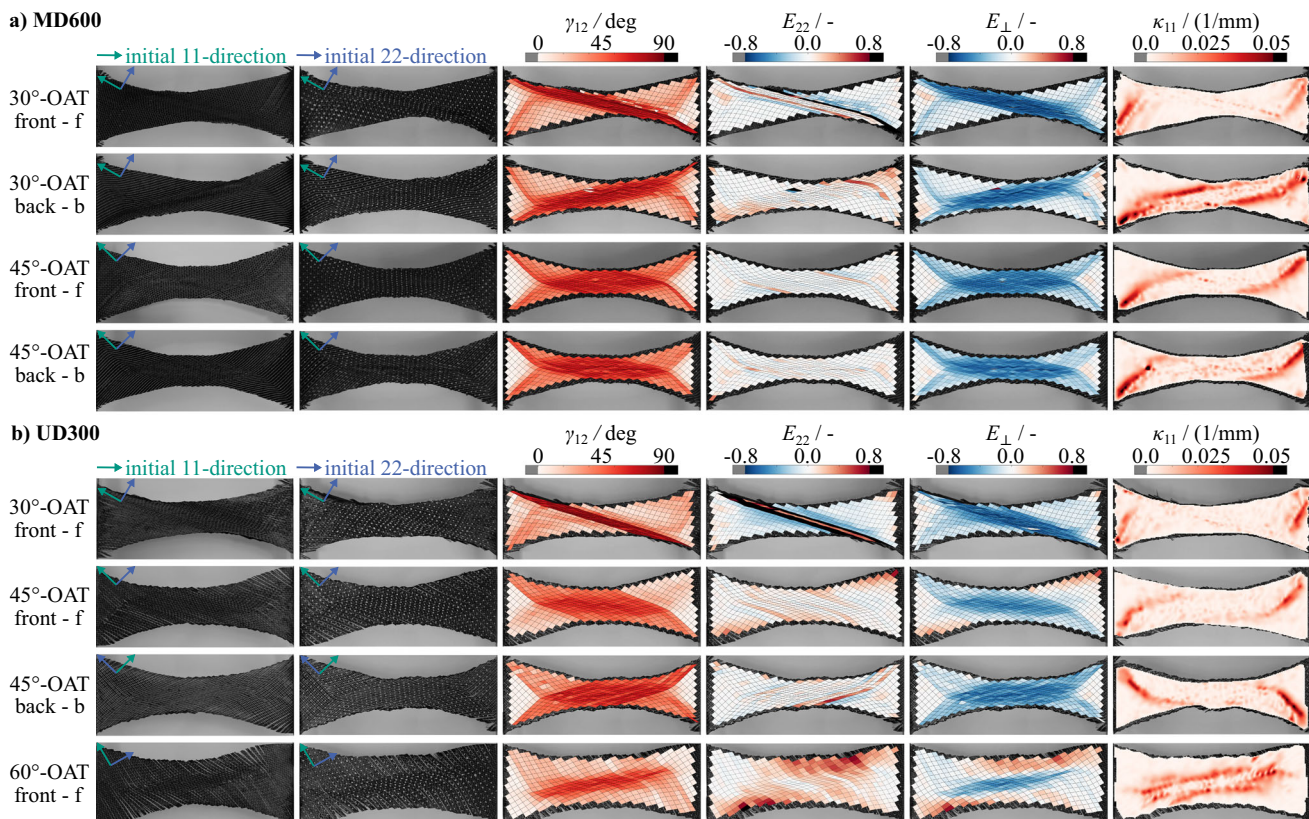


Fig. 8 Deformed specimens without (left) and without (second-left) dots as well as resulting strain distributions at an engineering strain of $\varepsilon = 0.25$ during Off-Axis-Tension tests (OATs) for medium-sized specimens (320 x 160 mm) of (a) Biax-NCF and (b) UD-NCF

the 45°-OAT and "B1" as well as "B2" in the 60°-OAT of the UD-NCF. In these areas, significant gaps develop between the rovings due to large stitching strains.

The strains in the MDZ of each test averaged over the areas highlighted in Fig. 3 a are shown for the Biax-NCF and UD-NCF in Fig. 9. The behavior of the Biax-NCF is mainly shear-dominated (γ_{12}) in the MDZ, which also induces perpendicular compaction E_{\perp} . Both increase relatively linear

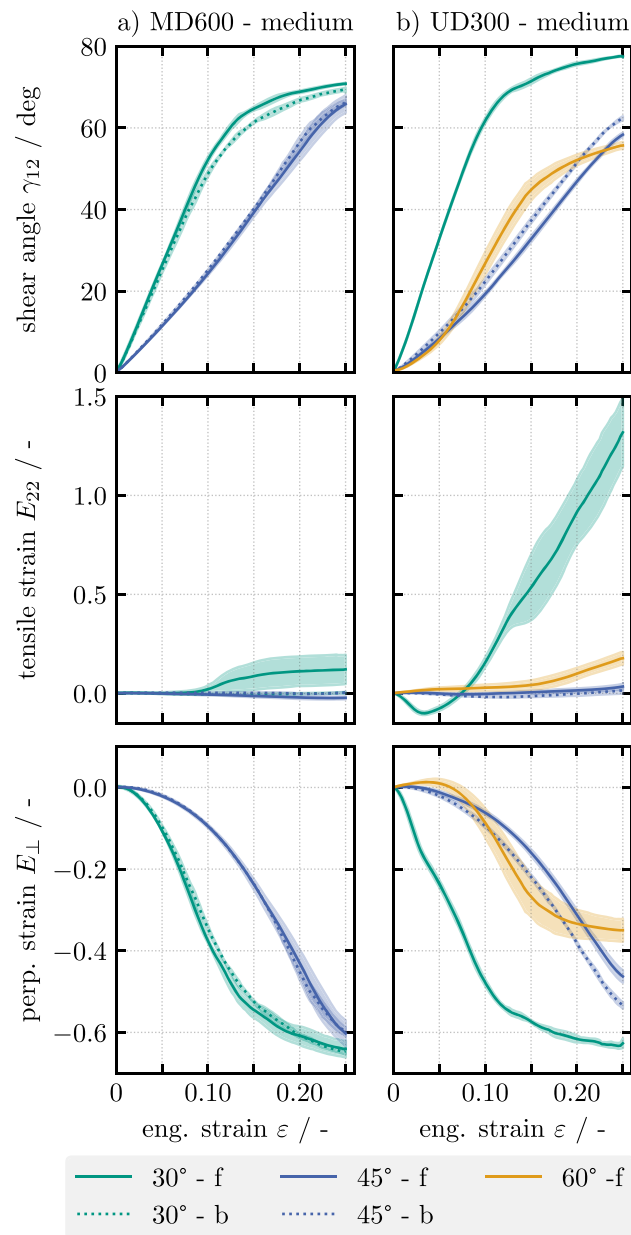


Fig. 9 Averaged strains in the MDZ of the OATs for medium specimens (320 x 160 mm) of the a) Biax-NCF (MD600) and b) UD-NCF (UD300)

until the textile for large $E_{\perp} < -0.4$ starts to exhibit the typical locking behavior, evident from the degressive curve of both strains. Due to the stitching, the rovings on the front and back side of the fabric are coupled resulting in similar E_{\perp} - as well as γ_{12} -strains in the 45°-OAT. On the front of the 30°-OAT positive transverse tensile deformation E_{22} occurs after the onset of locking, which indicates relative slipping of the rovings. Since the shear angle is only measured on the visible side of the NCF as a deformation of the dot pattern, this results in a slightly higher γ_{12} , cf. Eq. 1.

For the UD-NCF, different deformation states occur in the MDZ depending on the bias angle due to the different loading directions relative to the fiber orientation, cf. Fig. 9b. At the beginning of the 30°-OAT the rovings rotate towards the load direction, resulting in additional perpendicular compression which is not caused by shear as can be seen from the negative transverse tensile strains. Subsequently, large fiber slippage can be observed, causing large transverse tensile strains E_{22} superimposed with high shear strains γ_{12} and perpendicular compression E_{\perp} . As a result, the measured shear angle is significantly larger compared to the Biax-NCF while the maximum perpendicular compression is similar. In the 45°-OAT mainly shear deformation occurs in the MDZ, which is larger for the tests with the dot pattern on the back. This observation fits the greater influence of the dots when applying to the glass fiber side, which also resulted in less slippage, larger forces and larger necking, cf. Sections 4.2 and 4.3. In the early phase of the 60°-OAT the stitching is under high tension with simultaneously positive E_{22} - and E_{\perp} -strains. After $\epsilon \approx 0.075$, the MDZ starts to form in the center resulting in a strong increase in the shear angle and perpendicular compression. These flatten again for larger engineering strains since roving slippage starts as indicated by the increasing E_{22} -strain.

Based on the method described in Section 3.2, the roving curvature κ_{11} in the specimen can be measured, cf. Fig. 2. In the 30°-OAT the highest curvature occurs in the transition zones from "C" to "B2", but not necessarily between zones "B1" and "A" due to roving slippage. In the 60°-OAT for UD-NCF, cf. Fig. 8b, the gapping in zone "B2" prevents the formation of transition zones between "B3 and "C". This transition zone is observable for the 60°-oriented fibers on the back of the 30°-OAT for Biax-NCF. In general, the resulting curvatures are higher for Biax-NCF than for UD-NCF and the transition zones are larger. The second high-stiffness fiber direction prevents slippage and gapping along the edges. This improves the load transition resulting in higher in-plane moments and thus higher in-plane bending in the transition zones.

To evaluate the development of the roving curvature during the OATs the average of the maximum curvature $\bar{\kappa}_{11}^{\max}$ of

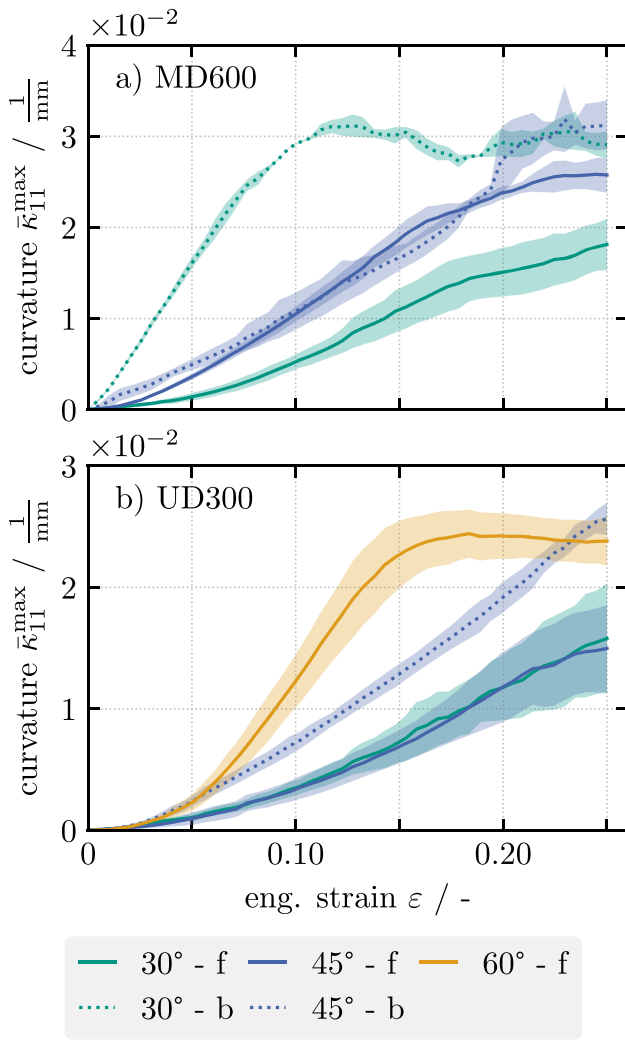


Fig. 10 Averaged curvature of the OATs for the a) Biax-NCF (MD600) and b) UD-NCF (UD300)

all measurement points n in each roving N^{rov} is calculated according to

$$\bar{\kappa}_{11}^{\text{max}} = \frac{1}{N^{\text{rov}}} \sum_{i=1}^{N^{\text{rov}}} \max_{n \in \{\text{roving}\}_i} \kappa_{11}(n). \quad (4)$$

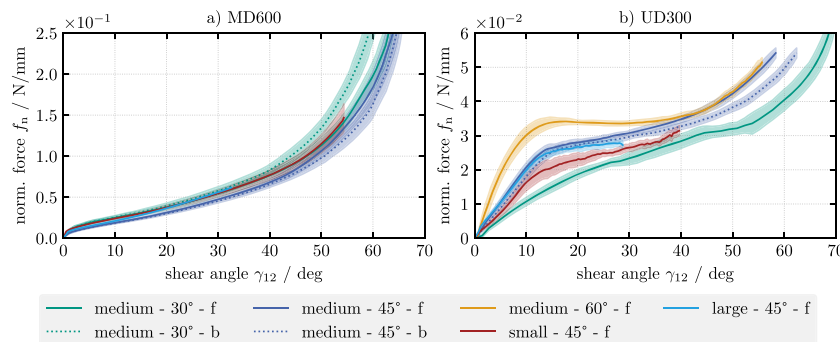


Fig. 11 Shear angle vs. force normalized by initial width for a) Biax-NCF (MD600) and b) UD-NCF (UD300)

The maximum curvature of each roving was chosen as a reference because it occurs in the transition zones, although these vary in size and location depending on the bias angle, cf. Fig. 2. The results are shown in Fig. 10. The average curvature shows slightly progressive trends for the 45°-OAT and the rovings on the front of the 30°-OAT. The curvature of the rovings with an initial orientation of $\Theta = 60^\circ$ in the 60°-OAT and on the back of the 30°-OAT of the Biax-NCF develops strongly degressive. In general, both materials show similar characteristic trends during the different OATs as already observed from the deformation images, although the average curvature for the Biax-NCF is higher in magnitude and increases earlier.

Comparison of 30°, 45°- and 60°-OATs

In order to better compare the different OATs with each other, the machine force normalized by the initial width, $f_n = f/w_0$, is shown as a function of the measured shear angle γ_{12} in Fig. 11. A calculation of the normalized shear force was deliberately omitted to allow comparison between the bias angles. Additionally, the classical assumption of a symmetrical shear behavior does not necessarily apply for NCF ($\gamma_{12}(\text{"A"})/2 \neq \gamma_{12}(\text{"B1"}) \neq \gamma_{12}(\text{"B2"})$) and the most common theories do not consider large slippage or transverse tensile strains [53]. However, the application of, for example, the three theories compared by Härtel et al [53] for the 45°-OAT would not change the relative position of the curves to each other and thus allow the same conclusions to be drawn.

Furthermore, 45°-OAT were performed on smaller specimens with $a_2^{\text{small}} = 160 \text{ mm}/80\text{mm}$ and on larger specimens for $a_3^{\text{large}} = 480 \text{ mm}/160\text{mm}$ to estimate an influence of the specimen size.

Pourtier et al. [34] have shown that for Biax-NCF a sufficiently large sample is required to obtain converged results, while this has not yet been investigated for UD-NCF. Details of the experiments and the deformations that occurred are given in Appendix A.

The behavior of the Biax-NCF is mainly shear-dominated independent of bias angle or the specimen size, cf. Section 4.4 and Appendix A. This results in a reasonable agreement of all 30°- and 45°-OAT within the range of experimental scatter for smaller γ_{12} and similar trends for larger γ_{12} , cf. Fig. 11 a. Only the results for the 30°-OAT with the strains measured on the back are notably higher, especially for higher shear angles. The results for the dot pattern on the front of the 30°-OAT would presumably also be higher without the observed roving slippage on the front, which increased the average shear angle, cf. Fig. 9 a.

The behavior of UD-NCF strongly depends on the stitching deformation, which results in a greater influence of the specimen size in the 45°-OAT, cf. Fig. 11 b. The results for medium and large specimens agree well within the tested range. However, the results for small specimens are noticeably lower, which can be attributed to observed slippage, gapping, and lack of roving bending, cf. Appendix A. This indicates a likely convergence of the measured behavior only for a sufficiently large specimen size, as also observed by Pourtier et al. [34] for Biax-NCF. The γ_{12} -related consideration also illustrates the influence of the bias-angle in the different OATs. In the early phase of the 60°-OAT the stitching is strongly tensioned and the slower increasing shear angle, cf. Fig. 9 b, leads to a higher initial slope. In contrast, the MDZ in the early phase of the 30°-OAT deforms under perpendicular compression, cf. Section 4.4. Thus, the stitching is not under tension and shear deformation is facilitated, resulting in a smaller initial slope.

Summary and discussion

The membrane behavior of fabrics under different ratios of superimposed shear, transverse tension and in-plane roving compaction can be investigated by different bias angles in OATs. Since NCFs do not adhere to either pure or simple shear theories, cf. Section 4.3, and only one fiber direction is visible from each side, a DIC measurement of the strains is essential for an accurate analysis. The DIC method used in this work introduces additional adhesion between the roving and the stitching through a dot pattern. This results in higher forces, cf. Section 4.2, but has only limited influence on the deformation behavior of the whole specimen and especially in the MDZ, cf. Section 4.3. However, the influence is relatively small compared to other methods [37]. By aligning the points along the rovings, the shear γ_{12} , transverse E_{22} and perpendicular E_{\perp} strains can be used to identify different deformation modes and to distinguish stitching deformation, roving slippage and gapping, cf. Fig. 4. In addition, a newly proposed method allows the measurement of fiber curvatures κ_{11} , which is neglected in most idealized theories, cf. Fig. 2.

The behavior of Biax-NCF is mainly shear-dominated with a minor asymmetry and only for large deformations

limited roving slippage can be observed. The shear angle γ_{12} in the 30°- and 45°-OAT increases nearly linearly in the beginning until the onset of locking for $E_{\perp} < -0.4$, cf. Figs. 9 and 12, which is also reflected in the resulting forces, cf. Figs. 5 and 11 a. Thus, the characterization of the shear properties is relatively independent of the specimen size and bias angle, cf. Fig. 11. The 30°-OAT mainly provides additional characterization opportunities regarding roving slippage and a different configuration of transition zones with higher fiber curvatures.

The behavior of UD-NCF strongly depends on the stitching deformation, resulting in a behavior characterized by superimposed shear, transverse tensile strains and perpendicular compression. In the 45°-OAT, the MDZ is mainly shear-dominated similar to the Biax-NCF, cf. Fig. 8. However, the behavior over the whole sample is strongly asymmetric and larger roving slippage is observable in combination with gapping in the edge regions of the secondary deformation zone. In addition, the results are distinctly dependent on the specimen size and a sufficiently large specimen is required to characterize a converged shear behavior, cf. Fig. 11 b. In the 30°- and 60°-OAT, positive transverse tensile strains are superimposed with shear deformation in the MDZ, indicating roving slippage that is not primarily limited to transition zones. This effect is much more pronounced in the 30°-OAT due to initial compression of the stitching and rovings, compared to the 60°-OAT, where tensioning of the stitching limits the shear deformation, cf. Fig. 9. In summary, it can be concluded that the 45°-OAT is presumably sufficient for a characterization of the shear behavior of UD-NCF. However, a complete characterization of the membrane behavior requires additionally the characterization of the transverse tensile and perpendicular compressive behavior as well as their interaction, which can be better understood by using different bias angles such as 30° and 60°. Furthermore, if the fiber bending stiffness of the rovings is to be taken into account, the different OATs also provide differently shaped transition zones and curvature amplitudes, cf. Figs. 8 and 10.

Conclusion

In this study, the membrane behavior of a UD- and a Biax-NCF is investigated under different multiaxial strain conditions with varying bias angles in off-axis-tension-tests (i.e. 30°, 45°- and 60°-OATs). A dot pattern is applied to the specimen to macroscopically measure the strains using DIC and a new method is developed to measure the fiber curvature as well. The OATs induce different ratios of large superimposed shear, transverse tensile and perpendicular compression deformation with a very simple and common setup. The 45°-OAT is best suited to characterize the shear

properties of both fabrics, as long as the sample size is large enough in the case of UD-NCF. The 30°- and 60°-OAT provide a better understanding of the transverse behavior. The Biax-NCF exhibits roving slippage and strong fiber bending at large deformations. In the UD-NCF, the membrane behavior is governed by the stitching load, which impedes shear deformation under tension and enhances shear as well as roving slippage under compression.

The results of the membrane behavior can be used for the parameterization of constitutive models and the development of new macroscopic simulation models. For Biax-NCF, current approaches are mainly based on the shear behavior [33, 56], which can be sufficiently determined based on the 45°-OAT. However, the results of a 30°-OAT will be useful for further developments that take into account roving slippage and in-plane fiber bending stiffness. In the case of UD-NCF, a characterization solely based on the 45°-OAT is not sufficient, since the complex interactions between fibers and stitching are not adequately explored with a single bias angle [36, 40]. Therefore, all three bias angles will be taken into account simultaneously in a future study to develop a new modeling approach. Subsequently, the development of methods to account for the in-plane fiber bending stiffness, based on accurate modeling of the transition zones, would be a possibility to account for the strongly anisotropic shear behavior parallel and transverse to the rovings in UD-NCF.

The application of the dot pattern on the back of the UD-NCF for DIC measurements, introduced additional adhesion between the stitching, glass fibers and rovings, resulting in a significant influence on the measured behavior. Thus, the influence of pressure in thickness direction on the membrane behavior of the UD-NCF should be investigated. In the presented tests, the glass fibers on the back side are only loosely coupled to the rovings by the stitching and barely contribute to the load transmission. Therefore, blankholders could have a significant influence on the membrane behavior, which is not accounted for in the characterization with OATs.

Appendix

A Investigation for different specimen sizes

The observed behavior in bias-extension tests (45°-OAT) can depend on the specimen size, as has been reported for unbalanced fabrics [9, 32] and Biax-NCF [34]. The influence of the specimen's size has not yet been investigated for UD-NCF. Therefore, additional tests with a bias angle of 45° were performed on smaller specimens for $a_2^{small} = 160\text{mm}/80\text{mm}$ and on larger specimens for $a_3^{large} = 480\text{mm}/160\text{mm}$. The larger specimens were only tested up to $\epsilon = 16.6\%$, due to a limited clamping length of the tensile testing machine.

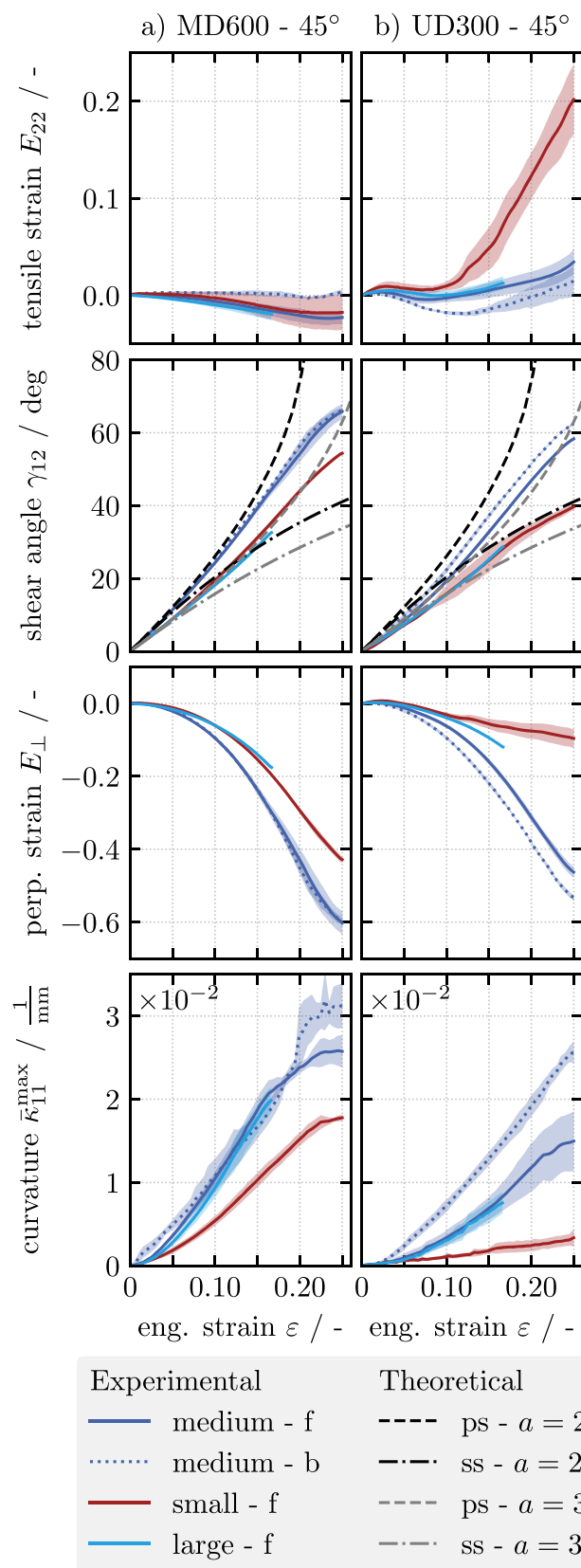


Fig. 12 Averaged strains in the MDZ and average roving curvature of the 45°-OAT for different specimen sizes of the a) Biax-NCF (MD600) and b) UD-NCF (UD300)

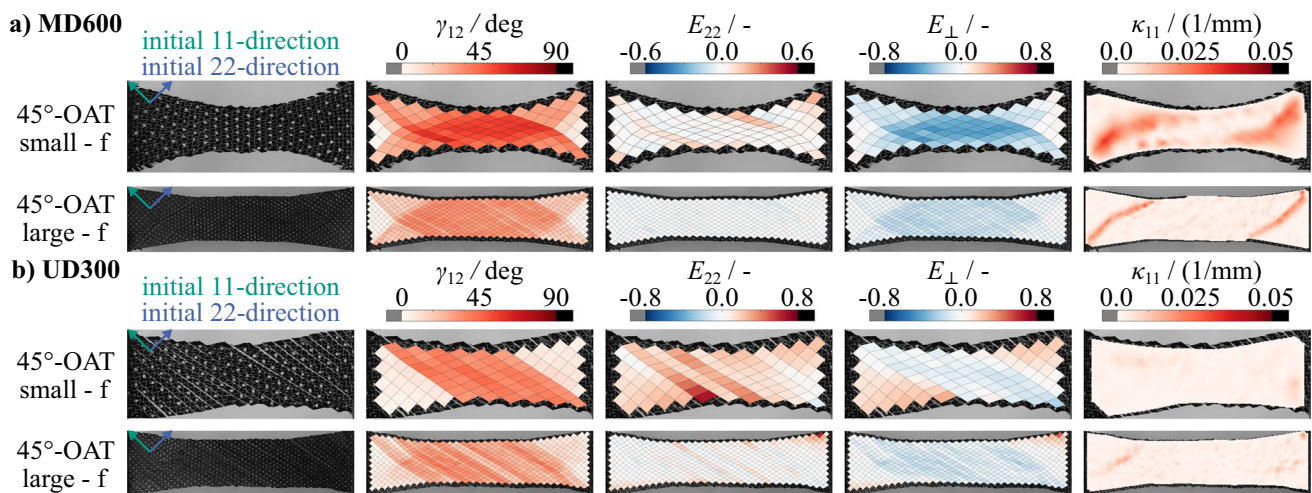


Fig. 13 Deformed specimens and strain distributions during Off-Axis-Tensions tests (OATs) (a) for Biax-NCF and (b) UD-NCF of different specimen sizes

The averaged strains in the MDZ and the average curvature are shown in Fig. 12 and the resulting strain distributions in Fig. 13. Additionally, the theoretical shear angles according to pure shear theory proposed by Cao et al. [9] and simple shear theory proposed by Pourtier et al. [34] are included for the averaged strains for both investigated aspect ratios.

The larger and smaller specimens of Biax-NCF show similar behavior to the medium specimen. The typical deformation zones, described in Section 4.1 are present with the highest deformation in the MDZ and measurable roving curvatures in the transition zones, cf. Figs. 12 a and 13 a. The behavior in the MDZ is mostly shear-dominated and the measured shear angle for medium and large specimens corresponds to the prediction according to a pure shear assumption for lower strains $\varepsilon < 0.1$, cf. Fig. 12 a. However, the measured shear angle of the small specimen is below the simple and pure shear prediction. The deviations are caused by slippage between the rovings in the transition area between zones "A" to "B1" and "B2" to "C". The effect is stronger for a smaller specimen size due to the relative size of a roving compared to the area of the MDZ.

The specimen size has a more pronounced effect on the observed behavior for UD-NCF. The larger specimens show the typical deformation zones but have a more inhomogeneous strain field, cf. Fig. 13 b. Due to the relatively loose stitching and the mesoscopic nature of the fabric, the load is not evenly distributed in the specimen. However, compared to the medium specimen similar averaged strains relative to the simple shear theory of their respective aspect ratios as well as averaged curvatures are measured, cf. Fig. 12b. In the smaller specimen, zones "B1" and "B2" are hardly pronounced and the fibers behave the same as in zones "A" and "C", respectively. The rovings bend significantly less and the

stitching is strongly tensioned, resulting in visible gaps and high transverse tensile strains E_{22} , cf. Fig. 13b. The effects described above are also reflected in the averaged strains in the MDZ, cf. Fig. 12b. Generally, the measured shear angle of all sizes for small strains is close to or below the simple shear theory, starting to exceed it for $\varepsilon > 0.1$ to 0.125 for medium and large specimens. For small specimens, γ_{12} remains below both theories due to the large transverse tensile strains E_{22} .

Acknowledgements The authors would like to thank the Deutsche Forschungsgemeinschaft (DFG, German Research Foundation) and the French National Research Agency (ANR) for funding the collaborative project "Composite forming simulation for non-crimp fabrics based on generalized continuum approaches" (project no. 431354059), which the presented work is carried out for. This work is also part of the Heisenberg project "Digitalization of fiber-reinforced polymer processes for resource-efficient manufacturing of lightweight components", funded by the DFG (project no. 455807141).

Author Contributions Bastian Schäfer: Conceptualization, Methodology, Validation, Formal analysis, Investigation, Data curation, Writing - Original Draft. Ruochen Zheng: Consulting, Writing - Review & Editing. Naim Naouar: Supervision, Writing - Review & Editing. Luise Kärger: Supervision, Conceptualization, Project administration, Funding acquisition, Writing - Review & Editing.

Funding Open Access funding enabled and organized by Projekt DEAL.

Declarations

Conflict of interest The authors declare that they have no conflict of interest.

Open Access This article is licensed under a Creative Commons Attribution 4.0 International License, which permits use, sharing, adaptation, distribution and reproduction in any medium or format, as

long as you give appropriate credit to the original author(s) and the source, provide a link to the Creative Commons licence, and indicate if changes were made. The images or other third party material in this article are included in the article's Creative Commons licence, unless indicated otherwise in a credit line to the material. If material is not included in the article's Creative Commons licence and your intended use is not permitted by statutory regulation or exceeds the permitted use, you will need to obtain permission directly from the copyright holder. To view a copy of this licence, visit <http://creativecommons.org/licenses/by/4.0/>.

References

- Galkin S, Kunze E, Kärger L, Böhm R, Gude M (2019) Experimental and Numerical Determination of the Local Fiber Volume Content of Unidirectional Non-Crimp Fabrics with Forming Effects. *J Composites Sci* 3(1). <https://doi.org/10.3390/jcs3010019>
- Kunze E, Galkin S, Böhm R, Gude M, Kärger L (2020) The Impact of Draping Effects on the Stiffness and Failure Behavior of Unidirectional Non-Crimp Fabric Fiber Reinforced Composites. *Materials* (Basel, Switzerland) 13(13). <https://doi.org/10.3390/ma13132959>
- Mei M, He Y, Yang X, Wei K, Qu Z, Fang D (2020) Shear deformation characteristics and defect evolution of the biaxial $\pm 45^\circ$ and $0/90^\circ$ glass non-crimp fabrics. *Compos Sci Technol* 193(3–4):108137. <https://doi.org/10.1016/j.compscitech.2020.108137>
- Kärger L, Galkin S, Kunze E, Gude M, Schäfer B (2021) Prediction of forming effects in UD-NCF by macroscopic forming simulation – Capabilities and limitations. Proceedings of the 24th international conference on material forming. <https://doi.org/10.25518/esaform21.355>
- Viisainen JV, Hosseini A, Sutcliffe MPF (2021) Experimental investigation, using 3D digital image correlation, into the effect of component geometry on the wrinkling behaviour and the wrinkling mechanisms of a biaxial NCF during preforming. *Compos A Appl Sci Manuf* 142(5):106248. <https://doi.org/10.1016/j.compositesa.2020.106248>
- Bussetta P, Correia N (2018) Numerical forming of continuous fibre reinforced composite material: A review. *Composites Part A: Applied Science and Manufacturing*. 113:12–31. <https://doi.org/10.1016/j.compositesa.2018.07.010>
- Liang B, Boisse P (2020) A review of numerical analyses and experimental characterization methods for forming of textile reinforcements. *Chinese J Aeronautics*. <https://doi.org/10.1016/j.cja.2020.09.027>
- Boisse P, Akkerman R, Carlone P, Kärger L, Lomov SV, Sherwood JA (2022) Advances in composite forming through 25 years of ESAFORM. *Int J Mater Form* 15(3):99. <https://doi.org/10.1007/s12289-022-01682-8>
- Cao J, Akkerman R, Boisse P, Chen J, Cheng HS, de Graaf EF et al (2008) Characterization of mechanical behavior of woven fabrics: Experimental methods and benchmark results. *Compos A Appl Sci Manuf* 39(6):1037–1053. <https://doi.org/10.1016/j.compositesa.2008.02.016>
- Boisse P (2015) Advances in composites manufacturing and process design. vol. number 56 of Woodhead publishing series in composites science and engineering. Cambridge, UK: Woodhead Publishing. Available from: <http://www.sciencedirect.com/science/book/9781782423072>
- Chen S, McGregor OPL, Harper LT, Endruweit A, Warrior NA (2016) Defect formation during preforming of a bi-axial non-crimp fabric with a pillar stitch pattern. *Compos A Appl Sci Manuf* 91:156–167. <https://doi.org/10.1016/j.compositesa.2016.09.016>
- Boisse P, Hamila N, Guzman-Maldonado E, Madeo A, Hivet G, dell'Isola F (2016) The bias-extension test for the analysis of in-plane shear properties of textile composite reinforcements and prepregs: a review. *Int J Mater Forming* p 1–20. <https://doi.org/10.1007/s12289-016-1294-7>
- Harrison P, Wiggers J, Long AC (2008) Normalization of Shear Test Data for Rate-independent Compressible Fabrics. *J Compos Mater* 42(22):2315–2344. <https://doi.org/10.1177/0021998308095367>
- Lomov SV, Boisse P, Deluycker E, Morestin F, Vanclooster K, Vandepitte D et al (2008) Full-field strain measurements in textile deformability studies. *Compos A Appl Sci Manuf* 39(8):1232–1244. <https://doi.org/10.1016/j.compositesa.2007.09.014>
- Schirmaier FJ, Weidenmann KA, Kärger L, Henning F (2016) Characterisation of the draping behaviour of unidirectional non-crimp fabrics (UD-NCF). *Compos A Appl Sci Manuf* 80:28–38. <https://doi.org/10.1016/j.compositesa.2015.10.004>
- Lebrun G, Bureau MN, Denault J (2003) Evaluation of bias-extension and picture-frame test methods for the measurement of intraply shear properties of PP/glass commingled fabrics. Selected Papers from the Symposium on Design and Manufacturing of Composites. 61(4):341–352. [https://doi.org/10.1016/S0263-8223\(03\)00057-6](https://doi.org/10.1016/S0263-8223(03)00057-6)
- Harrison P, Clifford MJ, Long AC (2004) Shear characterisation of viscous woven textile composites: a comparison between picture frame and bias extension experiments. *Compos Sci Technol* 64(10–11):1453–1465. <https://doi.org/10.1016/j.compscitech.2003.10.015>
- Harrison P, Tan MK, Long AC (2005) Kinematics of Intra-Ply Slip in Textile Composites during Bias Extension Tests. 8th Int ESAFORM Conf on Materials Forming
- Launay J, Hivet G, Duong AV, Boisse P (2008) Experimental analysis of the influence of tensions on in plane shear behaviour of woven composite reinforcements. *Compos Sci Technol* 68(2):506–515. <https://doi.org/10.1016/j.compscitech.2007.06.021>
- Hivet G, Duong AV (2011) A contribution to the analysis of the intrinsic shear behavior of fabrics. *J Compos Mater* 45(6):695–716. <https://doi.org/10.1177/0021998310382315>
- Aimène Y, Vidal-Sallé E, Hagège B, Sidoroff F, Boisse P (2010) A Hyperelastic Approach for Composite Reinforcement Large Deformation Analysis. *J Compos Mater* 44(1):5–26. <https://doi.org/10.1177/0021998309345348>
- Peng X, Guo Z, Du T, Yu WR (2013) A simple anisotropic hyperelastic constitutive model for textile fabrics with application to forming simulation. *Compos B Eng* 52:275–281. <https://doi.org/10.1016/j.compositesb.2013.04.014>
- Huang J, Boisse P, Hamila N, Gnaba I, Soulat D, Wang P (2021) Experimental and numerical analysis of textile composite draping on a square box. Influence of the weave pattern. *Composite Structures*, 267:113844. <https://doi.org/10.1016/j.compstruct.2021.113844>
- Creech G, Pickett A (2006) Meso-modelling of Non-Crimp Fabric composites for coupled drape and failure analysis. *J Mater Sci* 41(20):6725–6736. <https://doi.org/10.1007/s10853-006-0213-6>
- Li L, Zhao Y, Hgn Vuong, Chen Y, Yang J, Duan Y (2014) In-plane shear investigation of biaxial carbon non-crimp fabrics with experimental tests and finite element modeling. *Mater Des* 63:757–765. <https://doi.org/10.1016/j.matdes.2014.07.007>
- Ghazimoradi M, Trejo EA, Carvelli V, Butcher C, Montesano J (2021) Deformation characteristics and formability of a tricot-stitched carbon fiber unidirectional non-crimp fabric. *Compos A Appl Sci Manuf* 82:106366. <https://doi.org/10.1016/j.compositesa.2021.106366>
- Härtel F, Böhrer P, Middendorf P (2014) An Integral Mesoscopic Material Characterization Approach. *Key Eng Mater* 611–612:280–291. <https://doi.org/10.4028/www.scientific.net/KEM.611-612.280>

28. Wang J, Page JR, Paton R (1998) Experimental investigation of the draping properties of reinforcement fabrics. *Compos Sci Technol* 58(2):229–237. [https://doi.org/10.1016/S0266-3538\(97\)00115-2](https://doi.org/10.1016/S0266-3538(97)00115-2)
29. Bel S, Boisse P, Dumont F (2012) Analyses of the Deformation Mechanisms of Non-Crimp Fabric Composite Reinforcements during Preforming. *Appl Compos Mater* 19(3):513–528. <https://doi.org/10.1007/s10443-011-9207-x>
30. Bel S, Hamila N, Boisse P, Dumont F (2012) Finite element model for NCF composite reinforcement preforming: Importance of interply sliding. *Compos A Appl Sci Manuf* 43(12):2269–2277. <https://doi.org/10.1016/j.compositesa.2012.08.005>
31. Khiêm VN, Krieger H, Itskov M, Gries T, Stapleton SE (2016) An averaging based hyperelastic modeling and experimental analysis of non-crimp fabrics. *Int J Solids Struct*. <https://doi.org/10.1016/j.ijsolstr.2016.12.018>
32. Harrison P, Alvarez MF, Anderson D (2017) Towards comprehensive characterisation and modelling of the forming and wrinkling mechanics of engineering fabrics. *Int J Solids Struct*. <https://doi.org/10.1016/j.ijsolstr.2016.11.008>
33. Deghboudj S, Boukhedena W, Satha H (2018) Experimental and finite element analysis of in-plane shear properties of a carbon non-crimp fabrics at macroscopic scale. *J Compos Mater* 52(2):235–244. <https://doi.org/10.1177/0021998317704982>
34. Pourtier J, Duchamp B, Kowalski M, Wang P, Legrand X, Soulat D (2019) Two-way approach for deformation analysis of non-crimp fabrics in uniaxial bias extension tests based on pure and simple shear assumption. *Int J Mater Form* 12(6):995–1008. <https://doi.org/10.1007/s12289-019-01481-8>
35. Guzman-Maldonado E, Bel S, Bloom D, Fideu P, Boisse P (2022) Experimental and numerical analyses of the mechanical behavior during draping of non-orthogonal bi-axial non-crimp fabric composite reinforcements. *Mater Des* 218(3):110682. <https://doi.org/10.1016/j.matdes.2022.110682>
36. Schirmaier FJ, Dörr D, Henning F, Kärger L (2017) A macroscopic approach to simulate the forming behaviour of stitched unidirectional non-crimp fabrics (UD-NCF). *Compos A Appl Sci Manuf* 102:322–335. <https://doi.org/10.1016/j.compositesa.2017.08.009>
37. Trejo EA, Ghazimoradi M, Butcher C, Montesano J (2020) Assessing strain fields in unbalanced unidirectional non-crimp fabrics. *Compos A Appl Sci Manuf* 130:105758. <https://doi.org/10.1016/j.compositesa.2019.105758>
38. Krogh C, Kepler JA, Jakobsen J (2021) Pure and simple: investigating the in-plane shear kinematics of a quasi-unidirectional glass fiber non-crimp fabric using the bias-extension test. *Int J Mater Form* 19(3–4):1483–1495. <https://doi.org/10.1007/s12289-021-01642-8>
39. Ghazimoradi M, Trejo EA, Butcher C, Montesano J (2022) Characterizing the macroscopic response and local deformation mechanisms of a unidirectional non-crimp fabric. *Compos A Appl Sci Manuf* 156(9):106857. <https://doi.org/10.1016/j.compositesa.2022.106857>
40. Schäfer B, Haas S, Boisse P, Kärger L (2022) Investigation of the Membrane Behavior of UD-NCF in Macroscopic Forming Simulations. *Key Eng Mater* 926:1413–1422. <https://doi.org/10.4028/p-2977b4>
41. Lomov SV, Barbuski M, Stoilova T, Verpoest I, Akkerman R, Loendersloot R, et al. (2005) Carbon composites based on multi-axial multiply stitched preforms. Part 3: Biaxial tension, picture frame and compression tests of the preforms. *Composites Part A: Applied Science and Manufacturing* 36(9):1188–1206. <https://doi.org/10.1016/j.compositesa.2005.01.015>
42. Yu WR, Harrison P, Long A (2005) Finite element forming simulation for non-crimp fabrics using a non-orthogonal constitutive equation. *ACMC/SAMPE Conference on Marine Composites (MarComp) 2003* 36(8):1079–1093. <https://doi.org/10.1016/j.compositesa.2005.01.007>
43. Lee JS, Hong SJ, Yu WR, Kang TJ (2007) The effect of blank holder force on the stamp forming behavior of non-crimp fabric with a chain stitch. *Compos Sci Technol* 67(3–4):357–366. <https://doi.org/10.1016/j.compscitech.2006.09.009>
44. Pourtier J, Duchamp B, Kowalski M, Legrand X, Wang P, Soulat D (2018) Bias extension test on a bi-axial non-crimp fabric powdered with a non-reactive binder system. *AIP Conf Proc* 1960(1):020023. <https://doi.org/10.1063/1.5034824>
45. Krogh C, White KD, Sabato A, Sherwood JA (2020) Picture-frame testing of woven prepreg fabric: An investigation of sample geometry and shear angle acquisition. *Int J Mater Form* 13(3):341–353. <https://doi.org/10.1007/s12289-019-01499-y>
46. Lomov SV (2011) *Non-crimp fabric composites: Manufacturing, properties and applications*. Woodhead Publishing in materials. Oxford: Woodhead Publ. Available from: <http://site.ebrary.com/lib/alltitles/docDetail.action?docID=10654157>
47. Krieger H, Gries T, Stapleton SE (2018) Design of Tailored Non-Crimp Fabrics Based on Stitching Geometry. *Appl Compos Mater* 25(1):113–127. <https://doi.org/10.1007/s10443-017-9603-y>
48. Montesano J, Ghazimoradi M, Carvelli V (2023) Characterizing and modelling the coupled in-plane shear-biaxial tension deformation response of unidirectional non-crimp fabrics. *Int J Mater Form* 16(4):106857. <https://doi.org/10.1007/s12289-023-01757-0>
49. Ferretti M, Madeo A, dell’Isola F, Boisse P (2014) Modeling the onset of shear boundary layers in fibrous composite reinforcements by second-gradient theory. *Z Angew Math Phys* 65(3):587–612. <https://doi.org/10.1007/s00033-013-0347-8>
50. Steer Q, Colmars J, Naouar N, Boisse P (2021) Modeling and analysis of in-plane bending in fibrous reinforcements with rotation-free shell finite elements. *Int J Solids Struct* 222–223. <https://doi.org/10.1016/j.ijsolstr.2021.03.001>
51. Bogusz P (2023) Digital Image Correlation Analysis of Strain Fields in Fibre-Reinforced Polymer-Matrix Composite under $\pm 45^\circ$ Off-Axis Tensile Testing. *Polymers* 15(13). <https://doi.org/10.3390/polym15132846>
52. Pasco C, Khan M, Kendall K (2019) A novel discrete method of shear angle measurement for in-plane shear properties of thermoset prepreg using a point-tracking algorithm. *J Compos Mater* 53(14):2001–2013. <https://doi.org/10.1177/0021998318813193>
53. Härtel F, Harrison P (2014) Evaluation of normalisation methods for uniaxial bias extension tests on engineering fabrics. *Compos A Appl Sci Manuf* 67:61–69. <https://doi.org/10.1016/j.compositesa.2014.08.011>
54. Eberl C.: *Digital Image Correlation and Tracking*. MATLAB Central File Exchange. Available from: <https://www.mathworks.com/matlabcentral/fileexchange/12413-digital-image-correlation-and-tracking>
55. Belytschko T, Liu WK, Moran B, Elkhodary KI (2014) *Nonlinear finite elements for continua and structures*, 2nd edn. Wiley, Chichester
56. Bai R, Chen B, Colmars J, Boisse P (2022) Physics-based evaluation of the drapability of textile composite reinforcements. *Compos B Eng* 242(7):110089. <https://doi.org/10.1016/j.compositesb.2022.110089>